A new imaging method for understanding chemical dynamics: Efficient slice imaging using an in-vacuum pixel detector

J. H. Jungmann,[1] A. Gijsbertsen,[1] J. Visser,[2] J. Visschers,[2] R. M. A. Heeren,[1] and M. J. J. Vrakking[1,3]

[1]*FOM Institute for Atomic and Molecular Physics (AMOLF), Science Park 104, 1098 XG Amsterdam, The Netherlands*
[2]*National Institute for Subatomic Physics (Nikhef), Science Park 105, 1098 XG Amsterdam, The Netherlands*
[3]*Max-Born-Institut, Max Born Straße 2A, D-12489 Berlin, Germany*

The implementation of the Timepix complementary metal oxide semiconductor pixel detector in velocity map slice imaging is presented. This new detector approach eliminates the need for gating the imaging detector. In time-of-flight mode, the detector returns the impact position and the time-of-flight of charged particles with 12.5 ns resolution and a dynamic range of about 100 μs. The implementation of the Timepix detector in combination with a microchannel plate additionally allows for high spatial resolution information via center-of-mass centroiding. Here, the detector was applied to study the photodissociation of NO_2 at 452 nm. The energy resolution observed in the experiment was $\Delta E/E = 0.05$ and is limited by the experimental setup rather than by the detector assembly. All together, this new compact detector assembly is well-suited for slice imaging and is a promising tool for imaging studies in atomic and molecular physics research. © *2010 American Institute of Physics.* [doi:10.1063/1.3489890]

I. INTRODUCTION

Interest in imaging of reaction products of atomic and molecular collisions, of molecular photodissociation, and of photoionization events, has triggered the development of several imaging methods and detectors. The detection of the velocity distribution of fragments gives insight into the chemical reaction dynamics.

A well-established technique that is used in this context is velocity map imaging (VMI).[1,2] In this technique, charged particles, which are either created directly in the reaction or by the application of an ionization laser after the reaction, are extracted from the interaction region and accelerated by an electrostatic field toward a position-sensitive imaging detector (Fig. 1). The electrostatic optics of a typical VMI spectrometer consist of a repeller plate and a ring extractor plate that together create an electrostatic lens that is constructed such that particles with an identical initial velocity in the detector plane are mapped onto the same position on the detector, independent of their starting position in the interaction volume. Therefore, the impact position of a charged particle directly reflects its initial velocity vector in the detector plane.

The position-sensitive detector in a VMI spectrometer usually consists of a set of microchannel plates (MCPs), a phosphor screen, and a charge-coupled device (CCD) camera, which records the two-dimensional (2D) velocity distribution of the incident ions or electrons. If the detector plane contains an axis of cylindrical symmetry, the three-dimensional (3D) velocity distribution can be reconstructed from the 2D image via an inverse Abel transform.

Slice imaging is an imaging method, derived from VMI, that so far has only been applied to ions and that requires no mathematical reconstruction. In slice imaging, the detection is restricted to particles with a specific time-of-flight by rapidly switching the MCPs on and off. This allows one to exclude all particles from the measurement that have a nonzero velocity component perpendicular to the detector plane. Slice imaging exploits the dependence of the ion's arrival time on its initial velocity along the detector axis. These time-of-flight differences can be enhanced by using delayed pulsed extraction of the reaction products[3] or by applying very low voltages to the electrodes (dc slicing).[4] Typically, a time gate of 40 ns is applied to the detector.

Instead of a phosphor screen and a CCD camera, a delay-line detector or a wedge-and-strip anode[5] may be used to record the arrival time and position of electrons and ions. However, this approach necessarily poses limitations on the number of charged particles that can be detected per event/laser shot.[6] The reader is referred to Refs. 5 and 7 for an evaluation and comparison of the conventional, established detector approaches.

Here, we propose an alternative imaging detector concept relying on an in-vacuum pixel detector.[5] This hybrid pixelated complementary metal oxide semiconductor (CMOS) detector, a detector of the Medipix/Timepix family,[8–10] records (1) the position of impact of a particle and (2) the time-of-flight of this particle with respect to an external trigger with a maximum time resolution of 12.5 ns and a dynamic range of 13 bits (about 100 μs at the optimum time resolution). A typical Timepix detector arrangement consists of four chips comprising 256×256 pixels of 55×55 μm each. Every individual pixel provides the dual functionality of giving the impact position and the time-of-flight information of the impinging particles. In combination with a chev-
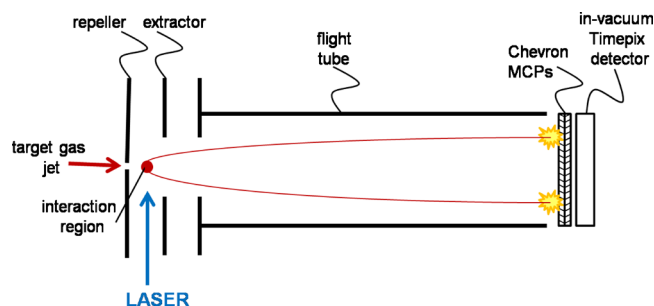
FIG. 1. (Color online) Schematic representation of the VMI spectrometer. The molecular beam and the photolysis laser intersect at right angles in between the repeller and extractor electrodes. The potentials applied on the electrodes accelerate the charged particles created in the interaction region toward the imaging detector. At the end of the flight tube, the composite MCP-Timepix detector assembly is mounted in-vacuum.

ron MCP stack, pixel detectors are capable of high-resolution, position-sensitive imaging of charged particles, where the spatial resolution can be better than the pixel size if an appropriate centroiding algorithm is used.[11] Conveniently, the implementation of a high time resolution, in-vacuum camera removes the need to gate the imaging detector in slice imaging. In this paper, a proof-of-principle slicing experiment on the photodissociation of NO_2 is presented. The results obtained demonstrate the utility of pixel detectors such as the Medipix/Timepix detector in slice imaging and, furthermore, pave the way for the use of this detector in high-repetition rate coincidence imaging experiments.

II. THE MEDIPIX/TIMEPIX DETECTOR FAMILY

The Medipix detector family has been developed within the Medipix collaboration hosted by the European Organization for Nuclear Research (CERN).[12] The Medipix2 (Refs. [8] and [9]) application-specific integrated circuit consists of a hybrid pixel detector with a combined sensor layer and read-out electronics. Every pixel has a 13 bits counter and can accommodate count rates of approximately 100 kHz for randomly arriving particles. The individual pixel size on the detector is 55×55 μm and one chip comprises an array of 256×256 pixels, providing an active area of ~ 2 cm^2. Here, a 2×2 array of chips with an active detector area of 28×28 mm^2 is used. The interested reader is referred to Refs. [5], [8], and [9] for a detailed description of the counting chip, different read-out interfaces, and file formats, as well as its implementation in photon, electron, and ion detection.

The Timepix chip[10] is derived from the Medipix2 chip design. The dimensions and geometry of the chip are equal to its predecessor counting chip, but the functionality on the pixel level is different. Each pixel can be individually selected to operate in one of three modes: (1) the counting mode, in which each pixel counts the number of particles it registers over a prescribed time interval; (2) the time-of-flight (TOF) mode, in which the arrival time of one particle is measured with respect to an external trigger/shutter signal (i.e., clock cycles are counted from the moment the particle arrives until the external shutter closes); and (3) the time-over-threshold (TOT) mode, in which the time is measured during which the charge deposited by the incoming particle

generates a voltage that exceeds the detection threshold level. If the Timepix chip is combined with a MCP stack, the TOT output gives the signal amplitude per pixel, i.e., a direct indication of the number of charges deposited on a Timepix pixel.

The minimum detectable charge per pixel is determined by the pixel's noise, i.e., by the "equivalent noise charge (ENC)."[13] In order to be well above the pixel's noise level, a minimum charge of $6 \times$ ENC is required to impinge on a pixel conventionally. The ENC per pixel is measured to be about 100 electrons for a bare chip and 113 electrons for a chip bump-bonded to a 300 μm silicon sensor layer. Thus, the minimum detectable charge is 6×100 electrons $= 600$ electrons for a bare chip pixel and 6×113 electrons $= 678$ electrons for a chip pixel with a 300 μm silicon sensor layer. When considering the overall chip minimum detectable charge, one quadratically adds the pixel-to-pixel threshold mismatch. A typical Timepix chip shows a pixel-to-pixel threshold mismatch of about 35 electrons if properly threshold equalized and a pixel-to-pixel threshold mismatch of about 250 electrons if it is not equalized. Therefore, a bare Timepix chip has a minimum detectable charge of $6 \times \sqrt{(100^2 + 35^2)} = 635$ (equalized chip) and $6 \times \sqrt{(100^2 + 250^2)} = 1616$ (nonequalized chip), respectively. A Timepix chip with a 300 μm silicon sensor layer has a minimum detectable charge of $6 \times \sqrt{(113^2 + 35^2)} = 710$ (equalized chip) and $6 \times \sqrt{(113^2 + 250^2)} = 1646$ (nonequalized chip), respectively.

The time resolution of these measurements depends on the clock speed applied via the read-out interface. For instance, a 2×2 Timepix chip array read by a MUROS2 interface[14] can be operated at a maximum clock speed of 80 MHz, resulting in a time resolution of 12.5 ns. Since the data are accumulated in a 13 bits counter per pixel, each pixel has a dynamic range of $2^{13} \times 12.5$ ns $= 102.4$ μs. Further information on the Timepix chip can be found in Refs. [5] and [10].

The TOF and TOT modes are particularly interesting for subpixel spatial resolution imaging provided an event is detected in multiple pixels. Particles can be registered by multiple pixels, for instance, via charge sharing between neighboring pixels.[15] It also naturally accompanies the use of a MCP in front of the Medipix/Timepix detector, when the detector records an electron shower consisting of thousands of electrons.[11] More details on the advantages of this approach are given below.

In our work, the 2×2 Timepix detector is read by means of the dedicated Medipix acquisition software PIXELMAN (Pixelman software, version 2007_07_24,[16]). Saved data files list the coordinates of pixels that have registered a count in combination with the value registered by the pixels: either the number of particles counted, or the moment it went over threshold, or the time it remained over threshold. The 2×2 Timepix is combined with a MUROS2 read-out interface.[14] This read-out interface is coupled to the Timepix printed-circuit board via an ultra SCSI (Small Computer System Interface) cable [Ultra 0.8 mm 68 male VHDCI (very high density cable interconnect) to Ultra 0.8 mm 68 male (VHDCI)]. The MUROS2 and the personal computer are interfaced by a National Instruments DIO-653X card. The maxi-

mum achievable read-out speed for a single chip is 160 Mbit/s, which yields a read-out time for the entire chip of about 6 ms.[14] Using a 2×2 bare Timepix array, we observe that the read-out speed depends on the number of chips in the array and the length of the read-out cable. In our experimental configuration, the typical read-out time amounts to 80 ms.

III. EXPERIMENTAL

In the experiment, a gas sample containing 10% NO_2 seeded in Ar is expanded into the source chamber via a homemade piezoelectric pulsed valve. The pulsed molecular beam passes through a skimmer into the spectrometer chamber. In this chamber, it is orthogonally crossed with a tuneable 452 nm laser beam, obtained from a Nd:YAG laser (Quanta-Ray DCR-3) and pumped by a dye laser (Spectra Physics PDL-3) with coumarin 47 dye. The repetition rate of the laser is 10 Hz and the pulse duration is 10 ns. The NO_2 molecules are photodissociated by two 452 nm photons. Subsequently, the NO photofragments are ionized via a (2+2) resonance enhanced multiphoton ionization (REMPI) scheme.

(1) $NO_2 + 2h\nu \rightarrow NO[X^2\Pi_\Omega(J'')] + O(^3P, {}^1D)$,

(2) $NO[X^2\Pi_\Omega(J'')] + 2h\nu \rightarrow NO[A^2\Sigma^+(J')]$,

(3) $NO[A^2\Sigma^+(J')] + 2h\nu \rightarrow NO^+ + e^-$.

The dissociation of NO_2 requires at least 3.11 eV. In this case both the NO fragments and the O fragments are left in their ground state. For oxygen, this is the $^3P_2$ state. Dissociation producing the oxygen $^3P_1$, $^3P_0$, or ^1D state requires an additional energy of 0.0196, 0.0281, and 1.9673 eV, respectively.[17] The maximum translational energy of the NO fragments (i.e., for ground-state NO) follows from the momentum and energy conservation and is 0.81–0.82 or 0.14 eV when the oxygen fragment is left in either one of the ^3P_j states or in the ^1D state, respectively.

The NO^+ ions are accelerated through the 10 cm flight tube toward the imaging detector. Voltages on the repeller and extractor were set to 1620 and 1670 V, respectively. The 2×2 bare Timepix detector is mounted approximately 2.5 mm behind a 4 cm diameter chevron MCP stack. It is desirable to minimize the distance between the MCP backside and the Timepix detector chips in order to minimize the spatial expansion of the MCP electron cloud, which determines the spatial resolution that can be obtained. Currently, the wire bonds of the chips limit reducing this distance. However, the resulting spatial expansion of the MCP cloud can be counteracted by applying appropriate potentials to the MCP frontside and backside. The pores of the MCP have a diameter of 12 μm on a 15 μm center-to-center spacing. In typical experiments, the MCP front and back sides are biased at voltages of −2.1 and −0.4 kV, respectively. The latter voltage is used to accelerate the electrons toward the Timepix detector that is at ground potential. Note that the flight tube is not at ground potential, but at the same potential as the front of the MCP stack.

In the current slicing experiment, an external shutter signal of 6 μs is applied to the detector (via the MUROS2 interface) at a repetition rate of 10 Hz. The shutter is syn-
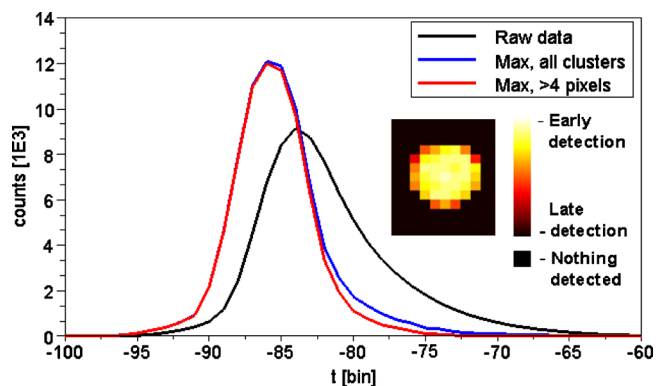

FIG. 2. (Color online) Time-of-flight spectrum of NO^+ fragments, after NO_2 photodissociation, and (2+2) REMPI at $\sim$451.64 nm and (1 bin = 12.5 ns). The raw data time-of-flight peak is based on the t measurements of the Timepix detector. This curve displays an "unphysical" asymmetry caused by the Timepix detector. This is mostly due to the charge sharing between pixels and a relationship between the charge deposited per pixel and the moment the pixel goes over threshold. The time resolution, and with that the symmetry of the peak, can be improved by selecting only the minimum tof pixel for clusters that correspond to the detection of a single particle. There also is a relation between the size of the cluster and the registered arrival time: on average, small clusters show a too late arrival. When omitting the clusters comprising four pixels or less, one can correct for the asymmetry in the TOF peak even more. Note that the "raw data" curve has been scaled by dividing the amount of pixels that fired by 23, the average cluster size.

chronized to the Q-switch of the Nd:YAG laser. The Timepix chips are operated in the TOF mode, which means that each pixel records the time t between the moment it went over threshold and the end of the shutter signal ($t_{shutter}$). In the remainder of this document, we will define the time axis by the convention $t_{shutter} = 0$. The time-of-flight of the detected particles is denoted by the tof, where tof $= t_{shutter} - t$.

Ions impinging on the MCP create an electron shower that shows up as a cluster of several pixels on the Timepix detector. A typical cluster for a single impact is depicted in the inset of Fig. 2. The color scale indicates the recorded time. Pixels that went over threshold earlier are colored light and the ones that went over threshold later are dark, while pixels that did not fire at all are black. There seems to be a relationship between the amount of charge deposited on a pixel and the moment the pixel goes over threshold, i.e., the more charge is deposited on a detector element, the earlier it goes over threshold. Therefore, pixels at the center of the MCP electron cloud footprint go over threshold first; pixels at the rim of the cluster go over threshold last. The typical time difference within a cluster (the difference between red and white pixels in the inset of Fig. 2) is 20 time bins. One clock cycle is 12.5 ns and thus this corresponds to 250 ns. The cluster is from a single ion impact and the observed temporal spread cannot be caused by the travel time through the MCPs, and from the MCPs to the Timepix detector, which is in the order of 1 ns.

The reduced time resolution is caused by charge sharing, i.e., the MCP charge cloud spans multiple pixels on the Timepix detector and divides its charge among those individual detector elements. This effect is reinforced in detectors where a semiconductor sensor layer in direct contact with the read-out chip is present. Here, the charge sharing is

amplified by the combined effect of the scattering and the diffusion of charge carriers in the silicon sensor.[15] The relative charge sharing between neighboring pixels depends on the impact particle energy[15] and the drift time in the semiconductor sensor layer,[18] which depends on the material characteristics of the sensor layer, the electric field bias and distribution across the sensor, and the interaction depth of the incident particle. The average size of a cluster can strongly be influenced by changing the MCP gain and the acceleration potential between the MCP back and the Timepix detector.

Since the time difference between ions that have their initial velocity toward, respectively, away from the detector is only of the order of a few 100 ns, the "raw" temporal resolution, as delivered by the Timepix, is insufficient for slicing experiments. The main plot in Fig. 2 displays the NO$^+$ time-of-flight trace based on the t measurements of the Timepix. Here, summed over 30 000 laser shots, the number of counts is given as a function of t in units of Timepix bins (12.5 ns). While the actual ion velocity distribution is symmetric along the time-of-flight axis, the observed time-of-flight peak is strongly asymmetric. This is due to the blurring introduced by charge sharing as described above.

To enhance the spatial resolution in our experiments, we applied a centroiding routine to the raw data. We use only the pixel in the cluster that went over threshold first to estimate the arrival time of the ion, while we use the "center-of-mass" of the cluster to calculate the position of impact via

$$C = \frac{\Sigma t_i r_i}{\Sigma t_i}.$$

Here, r_i is the coordinate corresponding to the center of pixel "i." The weights t_i are the difference between the arrival time on pixel i and the first arrival time that is not encountered anymore within cluster i (thereby giving pixels beyond the cluster boundary zero weight).

To enhance the temporal resolution, we used only used the minimum tof pixel for clusters (Fig. 2), i.e., the time recorded by the pixel that went over threshold first within a cluster. As expected, this peak is sharp and more symmetric than the raw data curve. However, a slight asymmetry can still be observed. This asymmetry can be traced back to a dependence of the measured arrival time of the electron cloud (and thus the ion) on the size of the cluster and can be reduced by omitting clusters consisting of four pixels or less. Such small clusters on average return "later" arrival times than clusters comprising more pixels, possibly due to a dependence of the charge migration time on the total amount of charge deposited. The red line in Fig. 2 shows the time-of-flight trace when selecting only the minimum tof pixel for clusters (as for the blue line) and also omitting clusters comprising less than five pixels. Clearly, the time-of-flight peak is much more symmetric, as it should be. All data shown in the remainder of this work were treated in this way. Note that for each ion impact (and resulting cluster of events on the Timepix detector) we store one arrival time, i.e., the minimum tof, and one set of arrival coordinates calculated via center-of-mass centroiding.

In the current experiment 30 000 acquisition frames were recorded. Due to the millisecond read-out time of the
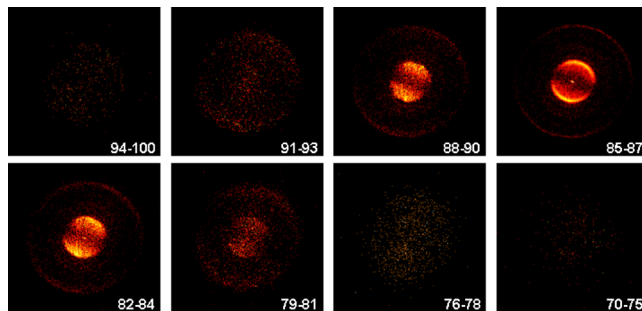

FIG. 3. (Color online) Series of slices through the NO$^+$ velocity distribution, recorded with a 2×2 Timepix detector and represented on a logarithmic color scale. Each impact position is calculated from the center-of-mass of the cluster, while the moment of impact is approximated by taking the moment when the first pixel within the cluster went over threshold. Clusters of less than 5 pixels were omitted. The data were binned onto a 512×512 matrix.

chips, the effective repetition rate of the experiment was 5 Hz and the acquisition lasted about 1.5 h. In one frame, the detector registered on average 2.6 events. The signal rate was limited to this value in order to keep the probability of double impacts at the same position low.

IV. RESULTS AND DISCUSSION

Figure 3 displays a series of slices through the NO velocity sphere after photodissociation of NO$_2$ at 451.64 nm. The numbers in the bottom corner of the images indicate the time-of-flight bins used to generate the images. Recall that each bin is 12.5 ns and that high numbers relate to early events. Bins 85–87 correspond to the center of the distribution (maximum of the symmetric curve in Fig. 2). The results in Fig. 3 demonstrate clearly that slices through the NO velocity distribution using the Timepix detector were successfully recorded.

Figure 4 displays the velocity distribution of the NO photodissociation fragments in the plane of the detector of the center slice (12.5 ns) and of the full (crushed) image, i.e., integrated over all the time bins. This corresponds to the in-plane velocity distribution observed in a common raw VMI image. The velocity distribution of the center slice is clearly sharper than the velocity distribution of the full data set. An image of the center slice (bin 86) is displayed in the
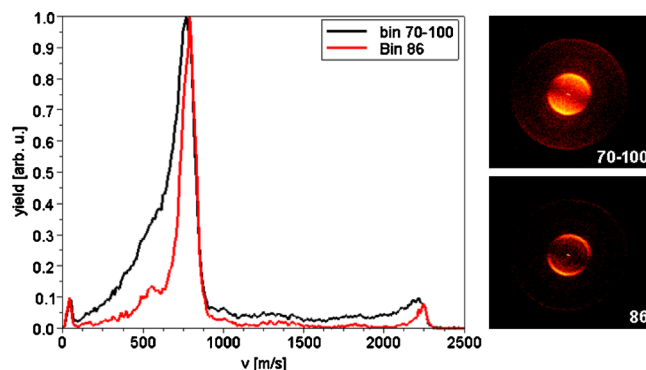

FIG. 4. (Color online) The left panel shows the in-plane velocity distribution of the center slice (corresponding to bin 86) and the integral over all slices (corresponding to bins 70-100). The right panel shows the ion images that correspond to the curves in the left panel.
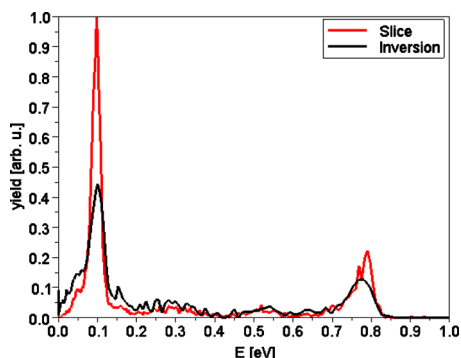
FIG. 5. (Color online) Kinetic energy distribution of the center slice (bin 86) and of the inverted integral image (bins 70–100). These curves follow from the momentum distributions in Fig. 4.

right panel of Fig. 4, along with the integrated image. The kinetic energy distribution, calculated from this slice, is compared in Fig. 5 to that obtained via an iterative inverse Abel transformation of the time-integrated image.[19] The overall shape of the two curves is similar. Still, the quality of the slice image is superior; the noise in the "inversion" (a result of the iterative inversion that recovers the 3D velocity distribution from the 2D projection) exceeds the noise in the slice. Noise in the experimental data is the most likely cause of the difference. A longer integration and thus reduction of the noise in the experimental image is expected to improve the correspondence between the result from the inversion and

from the slicing. Note that the centroiding algorithm in principle provides subpixel spatial resolution and the slicing result contains more bins than the result from the inverse Abel transform (1024 instead of 512).

The two peaks that dominate the spectrum (the two dominant rings in the images) correspond to the different states of the oxygen fragment. The peak at 0.8 eV (outer ring in the image) relates to the $NO[X^2\Pi_\Omega(J'')]+O(^3P_J)$ products, while the peak at 0.1 eV (inner ring) relates to the $NO[X^2\Pi_\Omega(J'')]+O(^1D)$ products which necessarily have a lower kinetic energy. Recall that the maximum kinetic energy of the NO fragments (when left in the ground state) is 0.82 eV when the oxygen fragment is left in one of the ^3P_J states and that it is 0.14 eV when the O fragment is in the ^1D state. The signal besides the two main peaks is probably due to NO that, upon dissociation, is left in highly excited states.

The rotational state of the probed NO products can be resolved by tuning the dye laser wavelength. To calibrate the dye laser, the spectrum from a beam of rotationally cold NO was measured, after which a spectrum of NO from NO_2 dissociation was recorded. Both spectra are plotted in Fig. 6 and compared to simulated spectra.[20] For reference purposes, the spectrum for NO from dissociation is compared to a two photon $A \leftarrow X$ spectrum for $NO(v=0)$ simulated at 300 K. We assume that in this wavelength range, ionization via the $A\,^2\Sigma^+$ state dominates the spectrum. However, upon dissociation, NO may be left in very highly excited rotational and
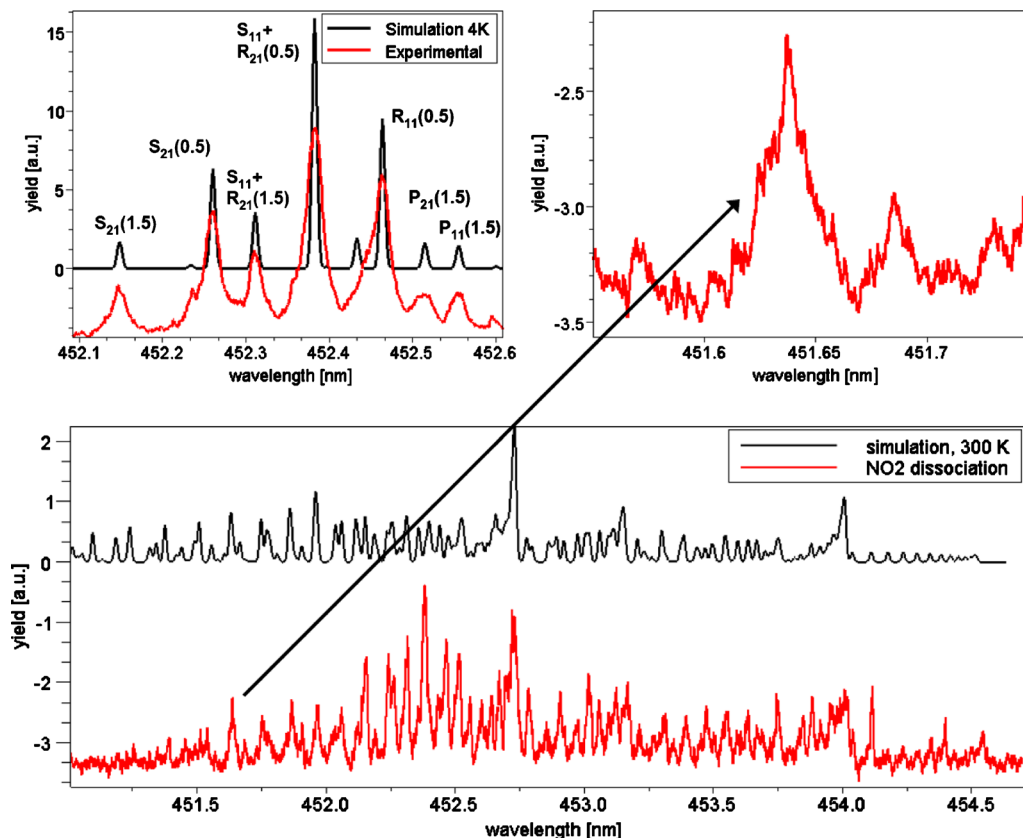

FIG. 6. (Color online) Simulated and experimental spectra are depicted as top and bottom trace, respectively. The top-left panel shows spectra for cold (4 K) NO and is used to calibrate our dye laser. The experimental data line in the bottom panel shows the spectrum for NO from NO_2 dissociation, while the top-right panel zooms in on the peak at which the experiment is performed. As a reference, a simulated two-photon absorption spectrum for NO at 300 K is provided (top curve in the bottom panel).

TABLE I. List of $A \leftarrow X$ transitions that may be probed around 451.64 nm.

λ (nm)	Transition $(\Delta N, \Delta J, F'', F', J'')$	Position (eV)			
		^1D	$^3P_2$	$^3P_1$	$^3P_0$
451.627	$sS_{11}(8.5) + sR_{21}(8.5)$	0.132	0.817	0.81	0.807
451.634	$tS_{21}(5.5)$	0.136	0.82	0.813	0.81
451.647	$rR_{22}(17.5) + rS_{12}(17.5)$	0.109	0.793	0.786	0.783

vibrational states and ionization may occur via different intermediate states than just the A state,[20] which means that the actual spectrum is more complex than the simulated one to which it is now compared. Roughly speaking, the right part of the spectrum in the bottom panel of Fig. 6 corresponds to NO in low rotational levels of the $^2\Pi_{3/2}$ state which is formed in the NO_2 dissociation, while the left part corresponds to NO in the $^2\Pi_{1/2}$ state. Around 452.4 nm, the spectrum shows the signature of some cold NO that is contained in the NO_2 molecular beam. The current experiments were performed at 451.64 nm at the top of the peak that is depicted in the top-right panel of Fig. 6. This peak has a width of approximately 0.03 nm.

Within the peak at 451.64 nm, a few rotational states of $NO(v=0)$ may be probed. The most likely spectroscopic transitions are provided in Table I with the recoil energy of the corresponding NO fragments. The comparison of the experimental spectrum from photodissociation of NO_2 with a simulated 300 K spectrum of NO (Fig. 6) suggests an important role for $NO(J''=8.5)$ and $NO(J''=5.5)$ in the experiment. However, this does not fit with the energy distribution observed in Fig. 5. The first peak should, in that case be, at 0.14 eV and not at 0.10 eV as is the case in the current experiment. The latter number does fit reasonably well to the $R_{22} + S_{12}(17.5)$ transition which should be found within the same peak (see Table I and Fig. 6).

The signal besides the two main peaks in Fig. 5 is most likely due to the NO in highly rotationally and vibrationally excited states. The spectrum is very dense and hence it is difficult to select a single rotational state of NO. Recently, Wilkinson *et al.*[21] studied NO_2 dissociation in a slice imaging experiment similar to ours, but using a single photon of 226 nm for dissociation, one for excitation and one for ionization. Although their results are dominated by NO fragments in relatively low rotational levels ($J''<21$) of the vibrational ground state that ionize via the $A\ ^2\Sigma^+$ intermediate state, they also observe signatures of highly rotationally and vibrationally excited states of NO. Ionization of NO molecules in vibrationally excited states ($v=5$ until $v=9$) at this wavelength proceeds via higher lying intermediate states.

The signal may have been influenced by the amplified spontaneous emission (ASE) in our laser beam, which may also cause some of the signal within the two main peaks in Fig. 5. ASE leads to a slight broadening of peaks in Fig. 5 toward lower energy because the experiment was performed close to the short-wavelength edge of the coumarin 47 wavelength range (444–476 nm when pumped with 355 nm light).

If one of the photons in the dissociation process originates from ASE, this leads to a broadening of 0.05 eV toward lower energy or 0.02 eV toward higher energy. In addition, photons from ASE may cause ionization of NO molecules in other than the selected state.

A better experiment with a higher quality (a narrower laser bandwidth and a lower level of ASE) would be needed to make definitive statements about the interpretation of the measured data and the underlying physics. For an elaborate discussion on the underlying physics, we refer to Ref. 20 and references cited therein.

The energy resolution in the current experiment is estimated to be $\Delta E / E = 0.05$ from the peak at 0.8 eV, which corresponds to 3 pixels or 165 μm on the detector. This number is most likely governed by (1) the ion optics and applied voltages thereon, (2) the simultaneous presence of several velocity components (see above), and (3) the fact that oxygen fragments in all three ^3P_J states contribute to this peak (leading to at most 0.01 eV energy difference of the NO atoms).

The experiment was performed at nonoptimal VMI conditions. The repeller and extractor electrodes carried relatively high voltages (<-1.6 kV), while the difference between the two electrodes was only 50 V. Recall that the flight tube and front of the detector was also at high voltage (-2.1 kV). As a result, the impact position on the detector may be more sensitive to the initial creation position of the ions than in optimized VMI conditions. Since the ionization volume can be approximated as a cylinder along the laser propagation direction with 1.5 mm length and 100 μm diameter, this effect can significantly contribute to the deterioration of the spatial resolution. This hypothesis is supported by the shape of the center spot in the bottom right panel in Fig. 4, which is stretched along the laser propagation axis and approximately measures 2×5 pixels (110×275 μm). This indicates nonideal VMI conditions and corresponds reasonably well with the observed experimental resolution (3 pixels). The voltages on the repeller and extractor were chosen such that the size of the center spot was as small as possible. It is the combination of the effects described above that leads to the observed resolution, rather than that of the Timepix detector itself.

V. CONCLUSIONS

In conclusion, we report the use of an MCP Timepix in-vacuum detector assembly for slice imaging. The combination of high-resolution, position-sensitive imaging and

time-of-flight measuring on the pixel level makes this detector a well-suited, simple, and attractive alternative to conventional ion imaging detector technology.

This new detector approach delivers a timing resolution of 12.5 ns per slice and, so far, an energy resolution of $\Delta E/E = 0.05$. Recently, Vallerga *et al.*[22,23] demonstrated that the spatial resolution of the Timepix detector in combination with MCPs can be pushed to 8.8 μm when operating the pixels in TOT mode, using a center-of-gravity centroiding algorithm and collecting sufficient statistics. This indicates that the Timepix detector (in combination with the MCP stack) bears outstanding spatial resolution capabilities and that the spatial resolution of the experiment presented here is limited by the experimental setup rather than by the detector approach itself. Still, in the presented experiment, the Timepix detector performs comparable to conventional slice imaging and inversion-algorithm based VMI.

The effective/raw time resolution was found to be worse than 12.5 ns. The measured arrival time within a cluster depends strongly on the position of a pixel in the cluster and also depends somewhat on the cluster size. This is due to the charge sharing of the MCP electron cloud between multiple pixels and to the amount of charge deposited on the individual pixel. This problem has successfully been addressed in this experiment. The relatively long readout time of the detector currently limits the experiment to 5 Hz, but this will be improved in the near future.

The Medipix/Timepix detector family has a large potential for gas-phase research in atomic and molecular physics in the near future. The work presented in Refs. 5 and 24 and the current work represent first steps toward this. An important next step will be coincident photoelectron and ion detection based on this type of in-vacuum pixel detector, in which the above mentioned difficulties and limitations are less relevant. The combination of the Timepix detector with an MCP and the Timepix's position-sensitive TOF and TOT functionality enable pixel spatial resolution via centroiding algorithms as well as timing information on the tens of ns level. Integrating this functionality and subnanosecond timing information from the MCP will enable the coincident detection of photoelectrons and ions in a simple, compact setup.

ACKNOWLEDGMENTS

[1] D. W. Chandler and P. L. Houston, J. Chem. Phys. **87**, 1445 (1987).
[2] A. T. J. B. Eppink and D. H. Parker, Rev. Sci. Instrum. **68**, 3477 (1997).
[3] C. R. Gebhardt, T. P. Rakitzis, P. C. Samartzis, V. Ladopoulos, and T. N. Kitsopoulos, Rev. Sci. Instrum. **72**, 3848 (2001).
[4] D. Townsend, M. P. Minitti, and A. G. Suits, Rev. Sci. Instrum. **74**, 2530 (2003).
[5] G. H. Gademann, Y. Huismans, A. Gijsbertsen, J. Jungmann, J. Visschers, and M. J. J. Vrakking, Rev. Sci. Instrum. **8**, 103 (2009).
[6] K. Ueda and J. H. D. Eland, J. Phys. B **38**, S839 (2005).
[7] J. S. Lapington, Nucl. Instrum. Methods Phys. Res. A **525**, 361 (2004).
[8] X. Llopart, M. Campbell, R. Dinapoli, D. San Segundo, and E. Pernigotti, IEEE Trans. Nucl. Sci. **49**, 2279 (2002).
[9] X. Llopart and M. Campbell, Nucl. Instrum. Methods Phys. Res. A **509**, 157 (2003).
[10] X. Llopart, R. Ballabriga, M. Campbell, L. Tlustos, and W. Wong, Nucl. Instrum. Methods Phys. Res. A **581**, 485 (2007).
[11] J. V. Vallerga, J. McPhate, A. Tremsin, O. Siegmund, B. Mikulec, and A. Clark, Nucl. Instrum. Methods Phys. Res. A **546**, 263 (2005).
[12] Website of the Medipix Collaboration, hosted by the European Center for Nuclear Research (CERN), collaboration spokesperson Michael Campbell, see www.cern.ch/medipix.
[13] X. L. Llopart, Ph.D. thesis, Mid Sweden University, 2007.
[14] D. San Segundo Bello, M. van Beuzekom, P. Janswijer, H. Verkooijen, and J. Visschers, Nucl. Instrum. Methods Phys. Res. A **509**, 164 (2003).
[15] K. Mathieson, M. S. Passmore, P. Seller, M. L. Prydderch, V. O'Shea, R. L. Bates, K. M. Smith, and M. Rahman, Nucl. Instrum. Methods Phys. Res. A **487**, 113 (2002).
[16] T. J. Holy, J. Jakubek, S. Pospisil, J. Uher, D. Vavrik, and Z. Vykydal, Nucl. Instrum. Methods Phys. Res. A **563**, 254 (2006).
[17] C. E. Moore, in *Tables of Spectra of Hydrogen, Carbon, Nitrogen, and Oxygen*, edited by J. W. Gallagher (CRC, Boca Raton, 1993).
[18] M. Maiorino, G. Pellegrini, G. Blanchot, M. Chmeissani, J. Garcia, R. Martinez, M. Lozano, C. Puigdengoles, and M. Ullan, Nucl. Instrum. Methods Phys. Res. A **563**, 177 (2006).
[19] M. J. J. Vrakking, Rev. Sci. Instrum. **72**, 4084 (2001).
[20] Website of PGOPHER, program for simulating rotational structure of molecules, see http://pgopher.chm.bris.ac.uk/ref.html.
[21] I. Wilkinson, M. P. de Miranda, and B. J. Whitaker, J. Chem. Phys. **5**, 131 (2009).
[22] R. Bellazzini, G. Spandre, M. Minuti, A. Brez, L. Baldini, L. Latronico, N. Omodei, C. Sgro, J. Bregon, M. Razzano, M. Pinchera, A. Tremsin, J. McPhate, J. V. Vallerga, and O. Siegmund, Nucl. Instrum. Methods Phys. Res. A **591**, 125 (2008).
[23] J. Vallerga, J. McPhate, A. Tremsin, and O. Siegmund, Nucl. Instrum. Methods Phys. Res. A **591**, 151 (2008).
[24] J. H. Jungmann, L. MacAleese, R. Buijs, F. Giskes, A. deSnaijer, J. Visser, J. Visschers, M. J. J. Vrakking, and R. M. A. Heeren, "Fast, high resolution mass spectrometry imaging using a Medipix pixelated detector," J. Am. Soc. Mass Spectrom. (to be pubished).